INTERNATIONAL JOURNAL FOR NUMERICAL METHODS IN FLUIDS
Int. J. Numer. Meth. Fluids 2002; **1**:1–27 *Prepared using* fldauth.cls *[Version: 2000/07/27 v1.0]*

Efficient, highly accurate *hp* adaptive finite element computations of the scattering width output of Maxwell's equations

P.D. Ledger[1,*] J. Peraire[2], K. Morgan[1], O. Hassan[1] and N.P. Weatherill[1]

[1] *School of Engineering, University of Wales, Swansea SA2 8PP, Wales, U.K.*
[2] *Department of Aeronautics and Astronautics, M.I.T., Cambridge, MA 02139, USA*

SUMMARY

A procedure is presented for the solution of electromagnetic wave scattering problems, employing triangular meshes and arbitrary order edge elements. A scattered field formulation is employed and the far field boundary condition is imposed by the use of a PML. An a–posteriori error estimation procedure is described that enables the bounding of the computed scattering width distribution. The error estimator is also employed to drive an adaptive mesh algorithm, either by increasing the element order or by decreasing the element size. Numerical examples, involving scatterers that are perfect electrical conductors, demonstrate the effectiveness of the methods.

KEY WORDS: electromagnetic scattering, frequency domain, arbitrary order edge elements, output error bounds, goal orientated adaptivity

1. INTRODUCTION

The $\mathcal{H}(\text{curl};\Omega)$ conforming finite element approximations for electromagnetics were introduced originally by Nédélec [1, 2, 3]. These elements are now more commonly known as edge elements and they have been the subject of much investigation, with the work of Monk [4, 5], who considered the analysis of various formulations including *hp* approximations with uniform p, being particularly important. Following this work, Demkowicz and co–workers [6, 7] developed a two dimensional hierarchical basis for edge elements, which enabled fully adaptive *hp* approximations to be undertaken on general domains. The approach adopted here follows these ideas, but employs instead the alternative form for the finite element shape functions defined recently by Ainsworth and Coyle [8]. This form has been shown to possess better conditioning properties and this is particularly important for high order implementations.

A typical area of application in the field of computational electromagnetics is the prediction of the scattering width distribution of two dimensional scatterers. Ainsworth and Coyle's higher order edge elements are known to provide an excellent framework for the solution of

*Correspondence to: School of Engineering, University of Wales, Swansea SA2 8PP, Wales, U.K. e–mail: cgledger@swansea.ac.uk

Received 30th April 2002
Revised ¡Date¿
Accepted ¡Date¿

such problems and a series of numerical examples has been presented which shows the approach to be an accurate method for predicting the scattering width [9]. Numerical convergence was demonstrated by repeated increase in the polynomial order, on a fixed mesh, until convergence of the scattering width distribution was achieved.

In this paper, we extend these ideas by incorporating an error estimation technique which is capable of approximating the level of accuracy of a given solution. To do this, we employ the a–posteriori error control approach of Patera, Peraire and coworkers [10]–[13], as this provides the ability to obtain inexpensive, sharp, rigorous and constant free bounds for the numerical error in engineering outputs of interest. The novel features of the work presented in this paper include the use of the scattering width as the output of interest and the extension to the use of arbitrary order elements. In addition, we investigate the effectiveness of an adaptivity approach that is driven by element contributions to the computed output bounds. A number of two dimensional scattering problems are solved to demonstrate the numerical performance of the proposed procedures.

2. PROBLEM STATEMENT

2.1. Governing equations

We are interested in simulating problems in which electromagnetic waves interact with an obstacle that is a perfect electrical conductor (PEC). It is assumed that the obstacle is

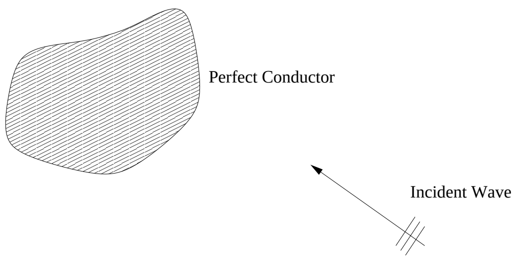

Figure 1. The electromagnetic scattering problem

surrounded by free space and that the waves are generated by a known source located in the far field. The problem is illustrated schematically in Figure 1. The unknowns are the electric and magnetic field intensity vectors, which are expressed relative to a cartesian coordinate system $Oxyz$, in the form $\boldsymbol{E} = (E_x, E_y, E_z)^T$ and $\boldsymbol{H} = (H_x, H_y, H_z)^T$ respectively. For scattering problems, it is convenient to decompose these fields into incident and scattered components, according to

$$\boldsymbol{E} = \boldsymbol{E}^i + \boldsymbol{E}^s \qquad \boldsymbol{H} = \boldsymbol{H}^i + \boldsymbol{H}^s \tag{1}$$

where the superscripts i and s denote the incident and scattered fields respectively. The governing equations are Maxwell's equations and, if a time variation $e^{\mathrm{i}\omega t}$ is assumed, the curl equations may be expressed in the dimensionless form

$$\mathrm{curl}\, \boldsymbol{E}^s = -\mathrm{i}\omega \boldsymbol{\mu}_f \boldsymbol{H}^s \qquad \mathrm{curl}\, \boldsymbol{H}^s = \mathrm{i}\omega \boldsymbol{\epsilon}_f \boldsymbol{E}^s \tag{2}$$

Prepared using fldauth.cls

and the divergence equations written as

$$\mathrm{div}\,(\boldsymbol{\epsilon}_f \boldsymbol{E}^s) = 0 \qquad \mathrm{div}\,(\boldsymbol{\mu}_f \boldsymbol{H}^s) = 0 \tag{3}$$

Here $\mathrm{i} = \sqrt{-1}$ and $\omega = 2\pi/\lambda$, where λ is the wavelength of the incident wave. The quantities $\boldsymbol{\mu}_f$ and $\boldsymbol{\epsilon}_f$ represent the relative permeability and relative permittivity respectively of the propagation medium. For general media, the entries in these tensors may be complex valued functions of position, but here, where the medium of propagation is free space, the tensors have the simple form

$$\boldsymbol{\mu}_f = \boldsymbol{I} \qquad \boldsymbol{\epsilon}_f = \boldsymbol{I} \tag{4}$$

where $\boldsymbol{I}$ is the unit tensor. We further restrict consideration to two dimensional problems, in which both $\boldsymbol{E}^s$ and $\boldsymbol{H}^s$ are functions of x and y only. For transverse electric (TE) simulations we have $\boldsymbol{E}^s = (E^s_x, E^s_y, 0)^T$ and $\boldsymbol{H}^s = (0, 0, H^s_z)^T$, while $\boldsymbol{E}^s = (0, 0, E^s_z)^T$ and $\boldsymbol{H}^s = (H^s_x, H^s_y, 0)^T$ for transverse magnetic (TM) problems.

2.2. Boundary conditions

2.2.1. PEC scatterer At the surface of a perfect electrical conductor, the scattered magnetic field is subject to the condition

$$\boldsymbol{n} \wedge \mathrm{curl}\,\boldsymbol{H}^s = -\boldsymbol{n} \wedge \mathrm{curl}\,\boldsymbol{H}^i \tag{5}$$

in TM simulations, where $\boldsymbol{n}$ represents the unit outward normal vector to the surface and $\wedge$ denotes the vector product. In this case, the surface of the scatterer is denoted by Γ_1. In TE

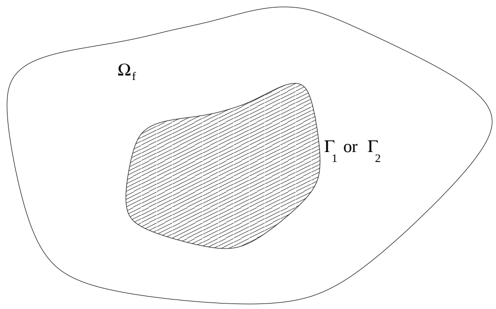

Figure 2. Creating the finite solution domain Ω_f

simulations, the scattered electric field is subject to the condition

$$\boldsymbol{n} \wedge \boldsymbol{E}^s = -\boldsymbol{n} \wedge \boldsymbol{E}^i \tag{6}$$

at the surface of the PEC scatterer and, in this case, this surface is denoted by Γ_2.

2.2.2. Far field treatment Sufficiently far from the scattering obstacle, the scattered electric and magnetic field components consist of outgoing waves only. Much attention has been devoted to the problem of developing a suitable implementation of this condition, as it is always encountered in the numerical simulation of wave propagation problems defined on infinite domains. When domain based methods are employed, the standard approach that is adopted involves the truncation, at a finite distance, of the infinite domain surrounding the scatterer to create a finite solution domain, Ω_f, as illustrated in Figure 2. A number of different methods may then be applied to handle the far field condition on the truncated domain but we employ Berenger's PML technique [14], as this has proved to be a particularly successful method [9]. In the PML approach, an artificial material layer, Ω_p, is added to the free space domain, Ω_f, at the truncated far field boundary, as shown in Figure 3. The outer surface of

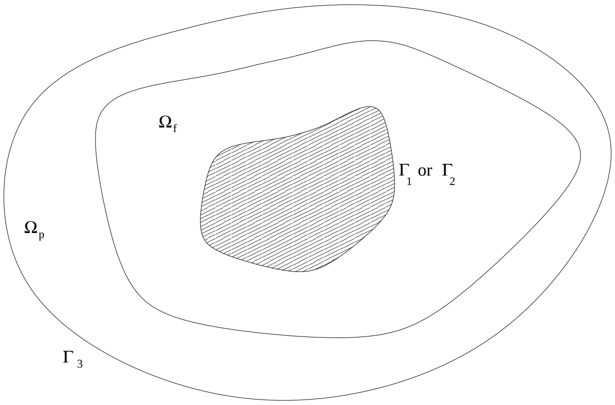

Figure 3. The addition of Ω_p, the PML region, to the domain Ω_f

the PML is denoted by Γ_3. Within the PML, Maxwell's curl equations are considered in the form

$$\mathrm{curl}\,\boldsymbol{E}^s = -\mathrm{i}\omega\boldsymbol{\mu}_p\boldsymbol{H}^s \qquad \mathrm{curl}\,\boldsymbol{H}^s = \mathrm{i}\omega\boldsymbol{\epsilon}_p\boldsymbol{E}^s \tag{7}$$

We attempt to choose the thickness of the PML, and to specify the variation of the material properties $\boldsymbol{\epsilon}_p$ and $\boldsymbol{\mu}_p$ through the PML, so that the outgoing wave condition is ensured by absorbing the scattered wave within the PML layer, with minimum reflection. At the outer surface, Γ_3, the boundary condition

$$\boldsymbol{n} \wedge \boldsymbol{E}^s = \boldsymbol{0} \tag{8}$$

is applied in TE simulations, while the condition

$$\boldsymbol{n} \wedge \boldsymbol{H}^s = \boldsymbol{0} \tag{9}$$

is applied in the TM case.

2.3. Variational formulation

By combining the free space and PML regions, the governing differential equation for this problem may be expressed in the form [9]

$$\mathrm{curl}\,\left(\boldsymbol{\Lambda}_1^{-1}\mathrm{curl}\,\boldsymbol{U}^s\right) - \omega^2\boldsymbol{\Lambda}_2\boldsymbol{U}^s = \boldsymbol{0} \tag{10}$$

where the unknown vector $\boldsymbol{U}^s$ is to be interpreted as the scattered electric field for the TE case and the scattered magnetic field in TM simulations. In addition, within Ω_f we take

$$\boldsymbol{\Lambda}_1 = \boldsymbol{\Lambda}_2 = \boldsymbol{I} \tag{11}$$

while in Ω_p

$$\boldsymbol{\Lambda}_1 = \boldsymbol{\mu}_p \qquad\qquad \boldsymbol{\Lambda}_2 = \boldsymbol{\epsilon}_p \tag{12}$$

for TE simulations and

$$\boldsymbol{\Lambda}_1 = \boldsymbol{\epsilon}_p \qquad\qquad \boldsymbol{\Lambda}_2 = \boldsymbol{\mu}_p \tag{13}$$

in the TM case. To develop a numerical solution procedure, a variational formulation of this problem is employed. The spaces

$$X^D = \{\boldsymbol{v} \,|\, \boldsymbol{v} \in \mathcal{H}(\mathrm{curl};\Omega);\ \boldsymbol{n}\wedge\boldsymbol{v} = -\boldsymbol{n}\wedge\boldsymbol{U}^i \text{ on } \Gamma_2;\ \boldsymbol{n}\wedge\boldsymbol{v} = \boldsymbol{0} \text{ on } \Gamma_3\} \tag{14}$$

$$X = \{\boldsymbol{v} \,|\, \boldsymbol{v} \in \mathcal{H}(\mathrm{curl};\Omega);\ \boldsymbol{n}\wedge\boldsymbol{v} = \boldsymbol{0} \text{ on } \Gamma_2,\ \boldsymbol{n}\wedge\boldsymbol{v} = \boldsymbol{0} \text{ on } \Gamma_3\} \tag{15}$$

are introduced and a weak variational formulation of the problem is then [9]: find $\boldsymbol{U}^s \in X^D$, such that

$$\mathcal{A}(\boldsymbol{U}^s, \boldsymbol{W}) = \ell(\boldsymbol{W}) \qquad\qquad \forall \boldsymbol{W} \in X \tag{16}$$

where

$$\mathcal{A}(\boldsymbol{U}^s, \boldsymbol{W}) = a(\boldsymbol{U}^s, \boldsymbol{W}) - \omega^2 m(\boldsymbol{U}^s, \boldsymbol{W}) \tag{17}$$

and

$$\ell(\boldsymbol{W}) = \int_{\Gamma_1} \boldsymbol{n}\wedge \mathrm{curl}\,\boldsymbol{U}^i \cdot \overline{\boldsymbol{W}}\,\mathrm{d}\Gamma \tag{18}$$

The bilinear forms that have been introduced here are defined as

$$a(\boldsymbol{U}^s, \boldsymbol{W}) = \int_{\Omega_f+\Omega_p} \mathrm{curl}\,\overline{\boldsymbol{W}} \cdot\ \boldsymbol{\Lambda}_1^{-1}\,\mathrm{curl}\,\boldsymbol{U}^s\,\mathrm{d}\Omega \tag{19}$$

$$m(\boldsymbol{U}^s, \boldsymbol{W}) = \int_{\Omega_f+\Omega_p} \overline{\boldsymbol{W}} \cdot\ \boldsymbol{\Lambda}_2\,\boldsymbol{U}^s\,\mathrm{d}\Omega \tag{20}$$

where the overbar denotes the complex conjugate. It might be expected that the enforcement of the divergence conditions of equation (3) would require the use of a Lagrange multiplier [6], with $\boldsymbol{U}^s$ in the above replaced by $\boldsymbol{U}^s + \mathrm{grad}\,p$, where $p \in \mathcal{H}^1(\Omega)$. However, for the scattering problems which are of interest here, which involve prescribed non zero values for ω, the resulting formulation would still reduce to equation (16) as the Lagrange multiplier, p, turns out to be identically equal to zero [7].

3. GALERKIN APPROXIMATION

A mesh of triangular finite elements is used to discretise the solution domain. In computational electromagnetics, extensive use has been made of the Whitney element [15], which is the lowest order triangular edge element. Edge elements give an approximation of the $\mathcal{H}(\text{curl};\Omega)$ space in which the tangential component of the solution is continuous across element edges. The level of accuracy for the Whitney element is low, as the tangential component of the solution is constant along each edge, so that fine meshes must be used for practical problems. Consequently, researchers have explored the use of higher order edge elements and Webb and Forghani [16] have presented a hierarchical scheme for triangular elements up to order four, in which the lowest order element is the Whitney element. Arbitrary order compatible quadrilateral and triangular edge elements were presented by Demkowicz and Rachowicz [6]. Recently, Ainsworth and Coyle [8] have developed a new family of compatible arbitrary order quadrilateral and triangular elements, which appear to have better conditioning properties, and it is their triangular elements which are adopted here. Discrete equations are produced by employing a Galerkin approximation to the variational statement of equation (16). Introducing the finite element subspaces X_H of X and X_H^D of X^D, the discrete form is: find $\boldsymbol{U}_H^s \in X_H^D$ such that

$$\mathcal{A}(\boldsymbol{U}_H^s, \boldsymbol{W}) = \ell(\boldsymbol{W}) \qquad \forall \boldsymbol{W} \in X_H \tag{21}$$

3.1. Triangular element basis functions

The master triangular edge element is taken to be the equilateral triangle with vertices located at the points $(1,0)$, $(0,\sqrt{3})$ and $(-1,0)$ in the (ξ,η) plane. Over this element, the variation of the unknown field is represented to order p as

$$\boldsymbol{U}^s(\xi,\ \eta) = \sum_{i=1}^{3}\sum_{j=0}^{p} e_j^i \boldsymbol{\phi}_j^i + \sum_{i=1}^{3}\sum_{j=0}^{p-2} e_{i,j}^{PI} \boldsymbol{\phi}_{i,j}^{PI} + \underbrace{\sum_{j=0}^{p-3}\sum_{k=0}^{p-3}}_{j+k\leq p-3} e_{j,k}^{GI_\xi} \boldsymbol{\phi}_{j,k}^{GI_\xi} + \underbrace{\sum_{j=0}^{p-3}\sum_{k=0}^{p-3}}_{j+k\leq p-3} e_{j,k}^{GI_\eta} \boldsymbol{\phi}_{j,k}^{GI_\eta} \tag{22}$$

In this expression, $\boldsymbol{\phi}$ denotes the vector form of the shape functions, while e denotes a scalar unknown. The basis functions $\boldsymbol{\phi}_j^i$ of order $j; j = 0, 1, \ldots, p$, are associated with the element edges $i; i = 1, 2, 3$, and involve the Legendre polynomials. For an efficient numerical implementation, a recursive relationship is used to generate the higher order terms [17]. The pseudo interior basis functions $\boldsymbol{\phi}_{i,j}^{PI}$, where $j = 0, 1, \ldots, p-2$, are added for $p \geq 2$. These functions are such that their tangential component vanishes on the triangle edges. Finally, the genuine interior basis functions $\boldsymbol{\phi}_{j,k}^{GI_\xi}$ and $\boldsymbol{\phi}_{j,k}^{GI_\eta}$ are also included for $p \geq 3$. These functions involve the Jacobi polynomials, which are also generated numerically by using a recursive relation [17]. We note that the genuine interior functions vanish completely on all the element edges.

3.2. PML treatment

An effective implementation of the PML for use with arbitrary order edge elements can be obtained by defining the PML parameters according to [9]

$$\boldsymbol{\epsilon}_p = \boldsymbol{\mu}_p = \boldsymbol{\Lambda} = \begin{bmatrix} \tilde{\boldsymbol{\Lambda}} & 0 \\ 0 & a \end{bmatrix} \tag{23}$$

where

$$a = 1 - (\mathrm{i}\sigma/\omega) \qquad\qquad \tilde{\boldsymbol{\Lambda}} = \boldsymbol{J}^T \begin{bmatrix} a & 0 \\ 0 & a^{-1} \end{bmatrix} \boldsymbol{J} \tag{24}$$

In this expression $\boldsymbol{J}$ denotes a rotation matrix [18] and σ is taken to vary quadratically with distance through the PML.

3.3. Geometrical details

A covariant mapping is employed to map each triangle in turn to the master triangular element [19]. In previous work [9], curved computational boundaries were approximated by straight line segments. Here, exact geometrical representation of the boundaries is achieved by the use of the linear blending function method [20].

3.4. Convergence rates

Monk [5] has derived an a–priori estimate for the convergence rates of three dimensional arbitrary order edge elements. To obtain this estimate, he used the lower order three dimensional edge elements of Nédélec [1, 2] and extended them to higher order. Ainsworth and Coyle [8] constructed their elements in a similar manner and Monk's estimate again holds. For uniformly spaced elements of size H and uniform order p, the estimate can be written in terms of the error in $\boldsymbol{U}^s$ as

$$\|\tilde{\boldsymbol{e}}\|_{\mathcal{H}^c} = \|(\boldsymbol{U}^s - \boldsymbol{U}^s_H)\|_{\mathcal{H}^c} \leq cH^{\min\,(p,t)} p^{-(t-1/2)} \|\boldsymbol{U}^s\|_{(\mathcal{H}_{t+1}(\Omega))^3} \tag{25}$$

where the $\mathcal{H}(\mathrm{curl};\Omega)$ norm is defined by

$$\|\tilde{\boldsymbol{e}}\|^2_{\mathcal{H}^c} = \int_\Omega \left(|\tilde{\boldsymbol{e}}|^2 + |\mathrm{curl}\,\tilde{\boldsymbol{e}}|^2\right) \mathrm{d}\Omega \tag{26}$$

and $\|\boldsymbol{U}^s\|_{(\mathcal{H}_{t+1}(\Omega))^3}$ denotes the usual Hilbert space norm. In equation (25), the parameter t depends on the regularity of the exact solution [21] and is large when the solution is smooth.

By studying the numerical convergence of a simple wave propagation problem with known analytical solution [22], the convergence rates of $\|\tilde{\boldsymbol{e}}\|_{\mathcal{H}^c}$ for the triangular edge elements can be investigated. The exact solution for this problem is smooth, so that $\min(p,t) = p$. For such smooth solutions, Monk's a–priori estimate indicates that an algebraic rate of convergence should be achieved for uniform mesh refinement with constant order elements. The numerical results that are presented in Table I demonstrate that this behaviour is observed in practice. The table shows the computed rate of convergence of $\|\tilde{\boldsymbol{e}}\|_{\mathcal{H}^c}$ for uniformly refined meshes, with a uniform polynomial order on each mesh. Here, $p = 0$ is a special case which produces the same linear rate of convergence as for $p = 1$. This can be explained by examining the dimension of the spaces from which the elements are constructed [8]. In general, the dimension of the

Prepared using fldauth.cls

Table I. Rates of convergence for the triangular elements with the mesh spacing H

p	0	1	2	3
$\|\|\tilde{\boldsymbol{e}}\|\|_{\mathcal{H}^c}$	1.00	1.00	1.97	2.95
$\mathcal{O}(H^p)$	-	1	2	3

space is $(p+1)(p+2)$, but for $p=0$ the dimension is 3. For values of $p \geq 1$ the predicted algebraic rates of convergence are achieved. In addition, if a mesh of uniformly spaced elements is enriched by uniformly increasing the polynomial order, an exponential rate of convergence is obtained [22].

We also consider at this stage, convergence rates measured according to the L_2 type norm

$$||\boldsymbol{w}||^2_{\mathcal{M}} = \int_\Omega |\boldsymbol{w}|^2 \, \mathrm{d}\Omega \tag{27}$$

and the semi norm

$$||\boldsymbol{w}||^2_{\mathcal{S}} = \int_\Omega |\mathrm{curl}\, \boldsymbol{w}|^2 \, \mathrm{d}\Omega \tag{28}$$

which is only semi positive definite. The computed convergence rates according to these norms,

Table II. Rates of convergence for $||\tilde{\boldsymbol{e}}||_{\mathcal{M}}$ and $||\tilde{\boldsymbol{e}}||_{\mathcal{S}}$ with the mesh spacing H

p	0	1	2	3
$\|\|\tilde{\boldsymbol{e}}\|\|_{\mathcal{M}}$	1.00	1.99	2.87	3.84
$\|\|\tilde{\boldsymbol{e}}\|\|_{\mathcal{S}}$	1.00	1.00	1.97	2.85

for the same wave propagation problem, are listed in Table II. In this table, it can be observed that the L_2 type norm, $||\tilde{\boldsymbol{e}}||_{\mathcal{M}}$ converges approximately at a rate that is $\mathcal{O}\left(H^{p+1}\right)$ with H, while the semi norm $||\tilde{\boldsymbol{e}}||_{\mathcal{S}}$ converges approximately at the rate of $\mathcal{O}\left(H^p\right)$ with H for $p>0$. Here, $p=0$ is again a special case, for which $||\tilde{\boldsymbol{e}}||_{\mathcal{M}}$ and $||\tilde{\boldsymbol{e}}||_{\mathcal{S}}$ both converge at the same rate.

The convergence rates investigated in this Section will be employed again later.

3.5. Computational outputs

When the Galerkin approximate solution has been established, the analyst is often interested in specific functional outputs of the computed solution. These outputs may be non linear or linear functionals of the solution $\boldsymbol{U}^s$ and, in addition, functions of another variable, ϕ. Here, we will consider real functional outputs, which we write as $s = \mathrm{Re}\{\mathcal{S}(\boldsymbol{U}^s;\phi)\}$. Ideally, we would like to compute this output on a very fine discretisation but, for many problems, this can be too expensive. It is, then, of interest to consider the possibilities offered by the process of a–posteriori error estimation, where the objective is to place upper and lower bounds on the output $s_H = \mathrm{Re}\{S(\boldsymbol{U}^s_H, \phi)\}$ computed on the working discretisation, X_H. At the outset, it should be noted that any regular non linear output functional may be linearised and expressed in the form

$$S(\boldsymbol{U}^s_H + \boldsymbol{w}; \phi) = S(\boldsymbol{U}_H; \phi) + \ell^{\mathcal{O}}(\boldsymbol{w}; \phi) + \mathcal{M}(\boldsymbol{w}, \boldsymbol{w}; \phi) \tag{29}$$

where $\ell^{\mathcal{O}}$ and $\mathcal{M}$ denote linear and non linear contributions respectively. We require that $\mathcal{M}$ be L_2 continuous and, in particular, that $|\mathcal{M}(\boldsymbol{w}, \boldsymbol{w}; \phi)| \leq C\|\boldsymbol{w}\|^2_{\mathcal{M}}$, where C is a constant that is independent of H. Before setting out the steps required for the error estimation process, it is convenient to introduce the bilinear forms

$$a^s(\boldsymbol{U}^s, \boldsymbol{W}) = \frac{1}{2}\left[a(\boldsymbol{U}^s, \boldsymbol{W}) + \overline{a(\boldsymbol{W}, \boldsymbol{U}^s)}\right] \tag{30}$$

$$m^s(\boldsymbol{U}^s, \boldsymbol{W}) = \frac{1}{2}\left[m(\boldsymbol{U}^s, \boldsymbol{W}) + \overline{m(\boldsymbol{W}, \boldsymbol{U}^s)}\right] \tag{31}$$

which are real when $\boldsymbol{W} = \boldsymbol{U}^s$. From these definitions, it is clear that

$$\mathcal{B}^s(\boldsymbol{U}^s, \boldsymbol{W}) = a^s(\boldsymbol{U}^s, \boldsymbol{W}) + \omega^2 m^s(\boldsymbol{U}^s, \boldsymbol{W}) \tag{32}$$

is such that $\mathcal{B}^s(\boldsymbol{W}, \boldsymbol{W})$ is also real and, when $\boldsymbol{\Lambda}_1$ and $\boldsymbol{\Lambda}_2$ are of the form given in equations (11)–(13), that $\mathcal{B}^s(\boldsymbol{W}, \boldsymbol{W})$ is also non negative for every $\boldsymbol{W}$.

4. CALCULATING ERROR BOUNDS

The procedure that has to be followed to compute upper and lower bounds for a specified output may be subdivided into a number of distinct steps. The process that is adopted here is an extension of an approach originally developed in the context of the Helmholtz equation [13].

Step 1 On the working mesh, obtain $\boldsymbol{U}^s_H \in X^D_H$, from

$$\mathcal{A}(\boldsymbol{U}^s_H, \boldsymbol{W}) = \ell(\boldsymbol{W}) \qquad \forall \boldsymbol{W} \in X_H \tag{33}$$

The residual

$$\mathcal{R}^U(\boldsymbol{W}) = \ell(\boldsymbol{W}) - \mathcal{A}(\boldsymbol{U}^s_H, \boldsymbol{W}) \tag{34}$$

is also defined and we note that $\mathcal{R}^U(\boldsymbol{W}) = 0 \; \forall \boldsymbol{W} \in X_H$.

Step 2 On the working mesh, compute an output adjoint $\Psi_H(\phi) \in X_H$ from

$$\mathcal{A}(\boldsymbol{W}, \Psi_H) = -\ell^{\mathcal{O}}(\boldsymbol{W}; \phi) \qquad \forall \boldsymbol{W} \in X_H \tag{35}$$

The adjoint residual

$$\mathcal{R}^\Psi(\boldsymbol{W}) = -\overline{\ell^{\mathcal{O}}(\boldsymbol{W}; \phi)} - \overline{\mathcal{A}(\boldsymbol{W}, \Psi_H)} \tag{36}$$

is also defined and again we note that $\mathcal{R}^\Psi(\boldsymbol{W}) = 0 \; \forall \boldsymbol{W} \in X_H$.

Prepared using fldauth.cls

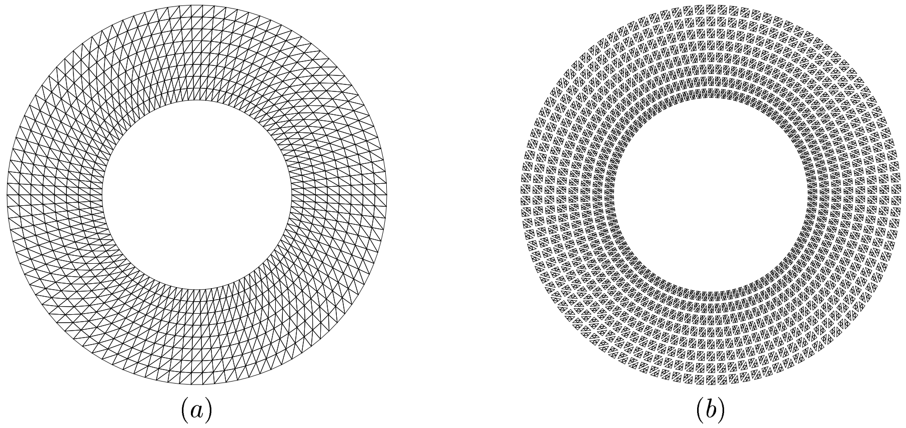

Figure 4. Simulation of an electromagnetic scattering problem showing (a) a typical working mesh and (b) a corresponding broken truth mesh

Step 3 A truth mesh is constructed by refinement of each coarse mesh triangle T_H. The refinement may be accomplished by either subdividing each triangle, or increasing the polynomial order of each triangle, or by a combination of both. Then, a coarse broken space is defined as

$$\hat{X}^H = \{\boldsymbol{v} |\ \boldsymbol{v} \in \mathcal{H}(\mathrm{curl};\Omega), \boldsymbol{v}|_{T_H} \in X_H(T_H), \forall T_H\} \tag{37}$$

and a corresponding broken truth space as

$$\hat{X}^h = \{\boldsymbol{v} |\ \boldsymbol{v} \in \mathcal{H}(\mathrm{curl};\Omega), \boldsymbol{v}|_{T_H} \in X_h(T_H), \forall T_H\} \tag{38}$$

This process is illustrated in Figure 4. When the broken spaces are introduced, edge fluxes are necessary to ensure that the solution computed on the broken elements remains in balance. Following Demkowicz [23], we achieve this by defining edge flux functionals λ^U and λ^Ψ according to

$$\lambda^U(\boldsymbol{W}) = \int_{\partial T_H} (\boldsymbol{n} \wedge \boldsymbol{W}) \cdot \boldsymbol{f}_H^U \,\mathrm{d}s \qquad \lambda^\Psi(\boldsymbol{W}) = \int_{\partial T_H} (\boldsymbol{n} \wedge \boldsymbol{W}) \cdot \boldsymbol{f}_H^\Psi \,\mathrm{d}s \tag{39}$$

and determine $\boldsymbol{f}_H^U, \boldsymbol{f}_H^\Psi \in \{\boldsymbol{n} \wedge \boldsymbol{W}|_{\partial T_H}, \boldsymbol{W} \in \hat{X}^H\}$ by requiring that

$$\lambda^U(\boldsymbol{W}) = \mathcal{R}^U(\boldsymbol{W}) \qquad \lambda^\Psi(\boldsymbol{W}) = \mathcal{R}^\Psi(\boldsymbol{W}) \tag{40}$$

for all $\boldsymbol{W} \in \hat{X}^H$.

Step 4 Reconstructed errors are computed in the decoupled truth space as

$$2\mathcal{B}^s(\hat{\boldsymbol{e}}^U, \boldsymbol{W}) = \mathcal{R}^U(\boldsymbol{W}) - \lambda^U(\boldsymbol{W}) \qquad \forall \boldsymbol{W} \in \hat{X}^h \tag{41}$$

$$2\mathcal{B}^s(\hat{\boldsymbol{e}}^\Psi, \boldsymbol{W}) = \mathcal{R}^\Psi(\boldsymbol{W}) - \lambda^\Psi(\boldsymbol{W}) \qquad \forall \boldsymbol{W} \in \hat{X}^h \tag{42}$$

and, then, we obtain

$$\hat{\boldsymbol{e}}^\pm = \hat{\boldsymbol{e}}^U \mp \frac{1}{\kappa}\hat{\boldsymbol{e}}^\Psi \tag{43}$$

where κ is a suitably defined scaling parameter.

Step 5 Finally, the required lower and upper bounds are computed as

$$s^- = \mathrm{Re}\{S(\boldsymbol{U}_H^s;\phi)\} - \kappa\mathcal{B}^s(\hat{\boldsymbol{e}}^-,\hat{\boldsymbol{e}}^-) \tag{44}$$

$$s^+ = \mathrm{Re}\{S(\boldsymbol{U}_H^s;\phi)\} + \kappa\mathcal{B}^s(\hat{\boldsymbol{e}}^+,\hat{\boldsymbol{e}}^+) \tag{45}$$

and, by choosing the scaling parameter, κ, according to [24]

$$\kappa = \sqrt{\frac{\mathcal{B}^s(\hat{\boldsymbol{e}}^\Psi,\hat{\boldsymbol{e}}^\Psi)}{\mathcal{B}^s(\hat{\boldsymbol{e}}^U,\hat{\boldsymbol{e}}^U)}} \tag{46}$$

these bounds are optimised.

4.1. Proof of bounding properties

To demonstrate that the quantities given in equations (44) and (45) are indeed valid lower and upper bounds on the prescribed output, we introduce the field variable error

$$\boldsymbol{e} = \boldsymbol{U}_h^s - \boldsymbol{U}_H^s \tag{47}$$

which is the difference between the truth and coarse mesh approximations. The truth mesh is regarded as being sufficiently fine so as to ensure that the output computed on the truth mesh, s_h, is indistinguishable from the exact output, s. Then, by combining equations (41) and (42) and choosing $\boldsymbol{W} = \boldsymbol{e}$, it follows that

$$2\kappa\mathcal{B}^s(\hat{\boldsymbol{e}}^-,\boldsymbol{e}) - \kappa\mathcal{A}(\boldsymbol{e},\boldsymbol{e}) - \overline{\ell^{\mathcal{O}}(\boldsymbol{e};\phi)} = 0 \tag{48}$$

and, in particular, that

$$Re[2\kappa\overline{\mathcal{B}^s(\hat{\boldsymbol{e}}^-,\boldsymbol{e})}] - \kappa Re[\overline{\mathcal{A}(\boldsymbol{e},\boldsymbol{e})}] + Re[\ell^{\mathcal{O}}(\boldsymbol{e};\phi)] = 0 \tag{49}$$

Expanding the left hand side, and adding the resulting equation to equation (44), it can be seen that

$$s^- = \mathrm{Re}\{S(\boldsymbol{U}_h;\phi)\} - \kappa\mathcal{B}^s(\boldsymbol{e}-\hat{\boldsymbol{e}}^-,\boldsymbol{e}-\hat{\boldsymbol{e}}^-) - \Big[\mathrm{Re}\left\{\mathcal{M}(\boldsymbol{e},\boldsymbol{e})\right\} - \kappa\mathcal{B}^s(\boldsymbol{e},\boldsymbol{e}) + \kappa\mathrm{Re}\{\overline{\mathcal{A}(\boldsymbol{e},\boldsymbol{e})}\}\Big] \tag{50}$$

and this may be simplified to

$$s^- = \mathrm{Re}\{S(\mathbf{U}_h;\phi)\} - \kappa\mathcal{B}^s(\mathbf{e}-\hat{\mathbf{e}}^-,\mathbf{e}-\hat{\mathbf{e}}^-) - \left[\mathrm{Re}\left\{\mathcal{M}(\mathbf{e},\mathbf{e})\right\} - 2\omega^2\kappa\mathrm{Re}\left\{m(\mathbf{e},\mathbf{e})\right\}\right] \tag{51}$$

on consideration of the properties of the bilinear forms $\mathcal{B}^s$ and $\mathcal{A}$. On the basis of the numerical experiments reported in Section 3.4, we believe that $\mathrm{Re}\left\{\mathcal{M}(\boldsymbol{e},\boldsymbol{e})\right\} - 2\omega^2\kappa\mathrm{Re}\left\{m(\boldsymbol{e},\mathbf{e})\right\}$ vanishes as $\mathcal{O}(H^{2(p+1)})$ for $p > 0$. This is much faster than $\kappa\mathcal{B}^s(\boldsymbol{e}-\hat{\boldsymbol{e}}^-,\boldsymbol{e}-\hat{\boldsymbol{e}}^-)$, which vanishes as $\mathcal{O}(H^{2p})$ and it follows that s^- will approach $\mathrm{Re}\{S(\boldsymbol{U}_h,\phi)\}$ from below, since $\mathcal{B}^s$ is positive definite. Similar arguments show s^+ to be an upper bound on $\mathrm{Re}\{S(\boldsymbol{U}_h,\phi)\}$.

5. SCATTERING WIDTH AS AN OUTPUT

For two dimensional electromagnetic scattering simulations, a non linear output which is of particular industrial interest is the scattering width, or the radar cross section per unit length. The evaluation of the scattering width requires the use of a near field to far field transformation and this is performed over a collection surface, Γ_c. The collection surface lies in the free space region, Ω_f, and totally encloses the scatterer. The scattering width, σ, which is a function of the viewing angle, ϕ, may then be evaluated as [15]

$$\sigma(\phi) = \frac{\omega}{4} \left| \int_{\Gamma_c} (\boldsymbol{n} \wedge \boldsymbol{U}^s \cdot \boldsymbol{V} + \boldsymbol{n} \wedge \mathrm{curl}\, \boldsymbol{U}^s \cdot \boldsymbol{Y}) \,\mathrm{d}\Gamma' \right|^2 \tag{52}$$

In this expression,

$$\boldsymbol{V} = \begin{bmatrix} 0 \\ 0 \\ \delta \end{bmatrix} e^{-\mathrm{i}\omega(x'\cos\phi + y'\sin\phi)} \qquad \boldsymbol{Y} = \frac{\delta}{\omega} \begin{bmatrix} -\sin\phi \\ \cos\phi \\ 0 \end{bmatrix} e^{-\mathrm{i}\omega(x'\cos\phi + y'\sin\phi)} \tag{53}$$

where δ is parameter which is equal to -1 for TE simulations and equal to $+1$ for TM computations. In discrete form, the scattering width integral of equation (52) is expressed as

$$\sigma_H(\phi) = \frac{\omega}{4} \left| \int_{\Gamma_c} (\boldsymbol{n} \wedge \boldsymbol{U}^s_H \cdot \boldsymbol{V} + \boldsymbol{n} \wedge \mathrm{curl}\, \boldsymbol{U}^s_H \cdot \boldsymbol{Y}) \,\mathrm{d}\Gamma' \right|^2 \tag{54}$$

and this may be evaluated once the Galerkin approximate solution $\boldsymbol{U}^s_H$ is determined. Note, however, that when using an edge element discretisation, $\mathrm{curl}\, \boldsymbol{U}^s_H$ is always approximated to a lower degree than $\boldsymbol{U}^s_H$. To compensate for this, Monk and coworkers [25]–[27] derived an alternative approach, in which the accuracy of the evaluation of the curl term is improved. In their approach, the term $\boldsymbol{n} \wedge \mathrm{curl}\, \boldsymbol{U}^s_H \cdot \boldsymbol{Y}$ in equation (54) is replaced by an area integral, over a layer of elements adjacent to Γ_c. This means that, in practice, the discrete integral in equation (54) is evaluated as [27]

$$\sigma_H(\phi) = \frac{\omega}{4} \left| \int_{\Gamma_c} (\boldsymbol{n} \wedge \boldsymbol{U}^s_H \cdot \boldsymbol{V}) \,\mathrm{d}\Gamma + \sum \int_k \left(\omega^2 \boldsymbol{U}^s_H \cdot \boldsymbol{y}_H - \mathrm{curl}\, \boldsymbol{U}^s_H \cdot \mathrm{curl}\, \boldsymbol{y}_H\right) \mathrm{d}\Omega \right|^2 \tag{55}$$

where the summation extends over all elements $k \in \Omega_f$, such that $\partial k \cup \Gamma_c \neq \emptyset$, and where $\boldsymbol{y}_H$ is chosen to be the edge element interpolation of $\boldsymbol{Y}$ on Γ_c and to be equal to zero at all interpolation points in Ω_f.

5.1. *Bounding the scattering width*

To evaluate bounds on the scattering width, we consider an output of the form

$$S(\boldsymbol{U}^s_H; \phi) = \mathcal{L}^{\mathcal{O}}(\boldsymbol{U}^s_H; \phi) \overline{\mathcal{L}^{\mathcal{O}}(\boldsymbol{U}^s_H; \phi)} \tag{56}$$

where

$$\mathcal{L}^{\mathcal{O}}(\boldsymbol{U}^s_H; \phi) = \int_{\Gamma_c} (\boldsymbol{n} \wedge \boldsymbol{U}^s_H \cdot \boldsymbol{V}) \,\mathrm{d}\Gamma + \sum \int_k \left(\omega^2 \boldsymbol{U}^s_H \cdot \boldsymbol{y}_H - \mathrm{curl}\, \boldsymbol{U}^s_H \cdot \mathrm{curl}\, \boldsymbol{y}_H\right) \mathrm{d}\Omega \tag{57}$$

It follows, from equation (55), that $S(\boldsymbol{U}^s_H;\phi) = 4\sigma_H(\phi)/\omega$. Linearisation of this output functional S gives

$$\ell^{\mathcal{O}}(\boldsymbol{w};\phi) = \mathcal{L}^{\mathcal{O}}(\boldsymbol{U}^s_H;\phi)\overline{\mathcal{L}^{\mathcal{O}}(\boldsymbol{w};\phi)} + \mathcal{L}^{\mathcal{O}}(\boldsymbol{w};\phi)\overline{\mathcal{L}^{\mathcal{O}}(\boldsymbol{U}^s_H;\phi)} \tag{58}$$

$$\mathcal{M}(\boldsymbol{w},\boldsymbol{w};\phi) = \mathcal{L}^{\mathcal{O}}(\boldsymbol{w};\phi)\overline{\mathcal{L}^{\mathcal{O}}(\boldsymbol{w};\phi)} \tag{59}$$

where $\mathcal{L}$ and $\mathcal{M}$ are the linear and nonlinear components respectively that are defined in equation (29). Before, we can evaluate bounds on $S(\boldsymbol{U}^s_H;\phi)$, we need to show that $|\mathcal{M}(\boldsymbol{w},\boldsymbol{w};\phi)| \leq C\|\boldsymbol{w}\|^2_{\mathcal{M}}$. To do this, a series of numerical experiments is undertaken, in which the convergence of $|\mathcal{M}(\boldsymbol{w},\boldsymbol{w};\phi)|$ is explored for a simple wave propagation problem with a known solution. The results, with $\boldsymbol{w} = \tilde{\boldsymbol{e}} = \boldsymbol{U}^s - \boldsymbol{U}^s_H$, are presented in Table III. Also

Table III. Convergence rates of $\mathcal{M}(\tilde{\mathbf{e}},\tilde{\mathbf{e}};\phi)$ compared to $\|\tilde{\mathbf{e}}\|^2_{\mathcal{M}}$

p	1	2	3
$\mathcal{M}(\tilde{\mathbf{e}},\tilde{\mathbf{e}};\phi)$	4.25	9.16	12.54
$\|\tilde{\mathbf{e}}\|^2_{\mathcal{M}}$	4	6	8

included in this table are the convergence rates of $\|\tilde{\boldsymbol{e}}\|^2_{\mathcal{M}}$, which are obtained from the results of the investigation undertaken in Section 3.4. From Table III, it is clear that the convergence rate of $|\mathcal{M}(\tilde{\boldsymbol{e}},\tilde{\boldsymbol{e}};\phi)|$ is faster than $\|\tilde{\boldsymbol{e}}\|^2_{\mathcal{M}}$ for $p = 1$, 2, 3. We expect similar behaviour will be exhibited for higher order elements and, therefore, we deduce that $\mathcal{M}(\boldsymbol{w},\boldsymbol{w};\phi)$ satisfies the desired condition. The evaluation of bounds on the scattering width now follows the general procedure outlined in Section 4.

6. NUMERICAL EXAMPLES OF BOUNDING COMPUTATIONS

Results of electromagnetic scattering simulations are presented which include the determination of bounds on the computed scattering width output. The selected problem is that of scattering of plane waves by a PEC circular cylinder of diameter $d = 2\lambda$. The computational domain is in the form of a circular annulus, with inner radius $r = \lambda$ and outer radius $r = 2\lambda$. The free space region, Ω_f, is defined by $\lambda \leq r \leq 1.25\lambda$ while the PML, Ω_p occupies the region $1.25\lambda \leq r \leq 2\lambda$. The spacing of the elements in the mesh is denoted by H. Ainsworth and Coyle [8] have investigated the dispersive effects of quadrilateral edge elements and have derived a discrete relationship between the true wave number ω and the computational wave number $\tilde{\boldsymbol{\omega}} = [\tilde{\omega}_x, \tilde{\omega}_y]^T$ in the form

$$\omega^2 - |\tilde{\boldsymbol{\omega}}|^2 = \frac{H^{2p}}{2p+1}\left[\frac{p!}{(2p)!}\right]^2 \left(\tilde{\omega}_x^{2p+2} + \tilde{\omega}_y^{2p+2}\right) + \mathcal{O}(H^{2p+2}) \tag{60}$$

Using this expression for triangular elements, with p replaced by $p+1$, should ensure a reasonably initial resolution of the waves. This argument is based on the fact that the error

Prepared using fldauth.cls

measured in the $\mathcal{H}(\text{curl};\Omega)$ norm for an order p quadrilateral element converges at a rate $\mathcal{O}(H^{p+1})$ compared to $\mathcal{O}(H^p)$ for an equivalently sized triangle of the same order [22]. For the simulations undertaken here, for a mesh of size H, the initial polynomial order is determined such that the inequality

$$\frac{H^{2(p+1)}}{2(p+1)+1}\left[\frac{(p+1)!}{(2(p+1))!}\right]^2\left(\tilde{\omega}_x^{2(p+1)+2}+\tilde{\omega}_y^{2(p+1)+2}\right)\leq 0.05\omega \tag{61}$$

is satisfied.

6.1. Fixed p

We consider the computation of the bounds on a series working discretisations for which the polynomial order is fixed and the mesh size is refined. An initial working mesh with average spacing $H = 0.31$ is selected and the dispersion relationship implies that elements of uniform order $p = 4$ should be employed. A mesh with average spacing $h = H/5$ is taken to be the truth mesh. The accuracy of the working discretisations, corresponding to $p = 4$ on different mesh spacings of H, $H/2$, $H/3$ and $H/4$ in turn, is investigated by computing bounds for $4\sigma_H(\phi)/\omega$ for viewing angles $\phi = 0$, 90 and 180 degrees. The collection surface, Γ_c, is taken to coincide with the surface of the scatterer and, for a TE simulation, the incident field is defined by

$$\boldsymbol{U}^i = -\omega^2\begin{bmatrix}0\\1\\0\end{bmatrix}e^{-\mathrm{i}kx} \tag{62}$$

Figure 5 shows the variation in the relative upper and lower bounds, s^+/s_h and s^-/s_h

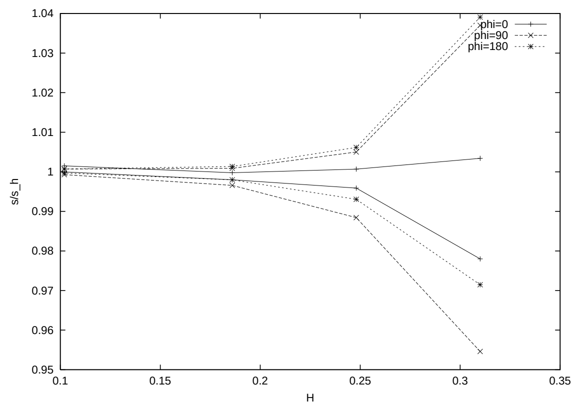

Figure 5. Scattering of a plane TE wave by a PEC circular cylinder of diameter $d = 2\lambda$: variation of s^+/s_h and s^-/s_h at $\phi = 0$, 90 and 180 degrees as the mesh is refined with p fixed

respectively, for this problem with decreasing mesh spacing H. It can observed that the magnitude of the relative bounds for $\phi = 0$ are tighter than those computed at $\phi = 90$ and $\phi = 180$, which implies that the accuracy of the output is most reliable at this location.

The incident field for the corresponding TM simulation is defined as

$$\boldsymbol{U}^i = \omega^2 \begin{bmatrix} 0 \\ 1 \\ 0 \end{bmatrix} e^{-\mathrm{i}kx} \tag{63}$$

and the same truth and working discretisations are adopted. Again, numerical bounds on the scattering width are determined at $\phi = 0$, 90 and 180 degrees and the results of the analysis

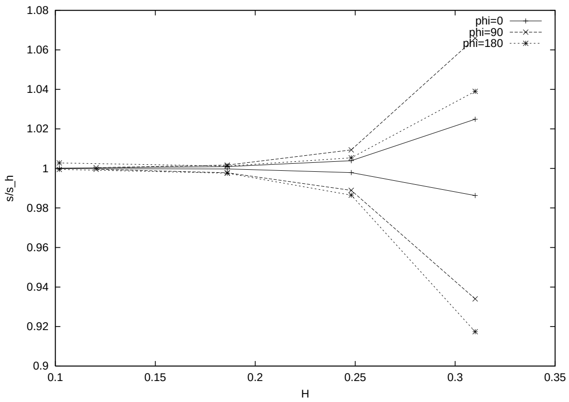

Figure 6. Scattering of a plane TM wave by a PEC circular cylinder of diameter $d = 2\lambda$: variation of s^+/s_h and s^-/s_h at $\phi = 0$, 90 and 180 degrees as the mesh is refined with p fixed

are shown in Figure 6. In this figure, we observe similar behaviour to the TE case, with $\phi = 0$ being the location where the output is most reliable.

6.2. *Fixed H*

Now we consider the computation of the bounds on a series working discretisations for which the mesh spacing is fixed but the polynomial order is continually increased. The initial mesh is again defined by the average spacing of $H = 0.31$ and with uniform element order $p = 4$. The truth discretisation for this example is selected as the mesh for which $h = 0.31$ and with uniform element order $p = 8$. The accuracy of a series of working mesh discretisations with a fixed mesh spacing and uniform polynomial orders of $p = 4$, 5, 6, 7 in turn is considered, with numerical bounds on the output $4\sigma_H(\phi)/\omega$ again determined at values of the viewing angle, ϕ, corresponding to 0, 90 and 180 degrees. The results of the TE simulation are displayed in Figure 7 and, as before, it is observed that the location $\phi = 0$ has the tightest bounds. By comparing Figure 7 and Figure 5, it can be seen that the bounds converge much more sharply when p is refined as opposed to refining H. In a similar manner, we consider the same truth and working mesh discretisations for the corresponding TM problem. The bounds obtained are shown in Figure 8 and the conclusions are similar to those reached when comparing the results of the TE computations.

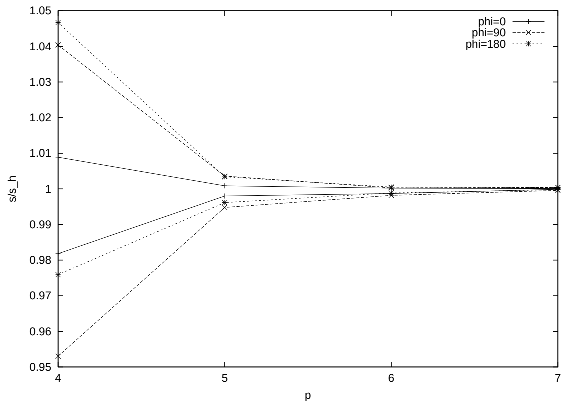

Figure 7. Scattering of a plane TE wave by a PEC circular cylinder of diameter $d = 2\lambda$: variation of s^+/s_h and s^-/s_h at $\phi = 0$, 90 and 180 degrees as p is increased with H fixed

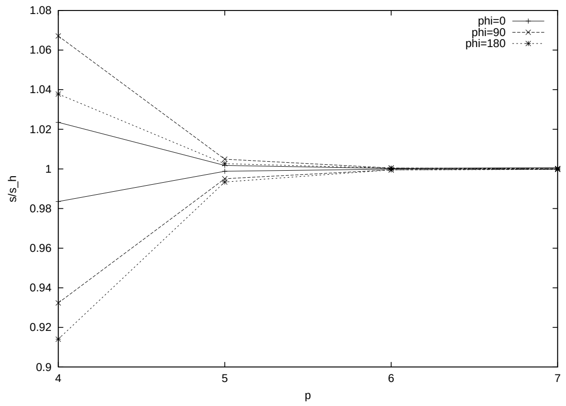

Figure 8. Scattering of a plane TM wave by a PEC circular cylinder of diameter $d = 2\lambda$: variation of s^+/s_h and s^-/s_h at $\phi = 0$, 90 and 180 degrees as p is increased with H fixed

7. AN ADAPTIVE ALGORITHM

Within this overall framework, it is now possible to implement an adaptive mesh algorithm for the simulation of electromagnetic wave scattering problems. The basic approach is to distinguish elements that should be flagged for refinement [24] and to this end, we define the parameter, Δ, that is related to the bound gap as

$$\Delta = \frac{1}{2}\left(s^+ - s^-\right) \tag{64}$$

It can be seen that

$$s^+ - s^- = \kappa \mathcal{B}^s(\hat{\boldsymbol{e}}^+, \hat{\boldsymbol{e}}^+) + \kappa \mathcal{B}^s(\hat{\boldsymbol{e}}^-, \hat{\boldsymbol{e}}^-) \tag{65}$$

and, since

$$\hat{\boldsymbol{e}}^{\pm} = \hat{\boldsymbol{e}}^{U} \mp \frac{1}{\kappa}\hat{\boldsymbol{e}}^{\Psi} \tag{66}$$

it follows that

$$\Delta_k = \kappa \mathcal{B}_k^s(\hat{\boldsymbol{e}}^U, \hat{\boldsymbol{e}}^U) + \frac{1}{\kappa}\mathcal{B}_k^s(\hat{\boldsymbol{e}}^\Psi, \hat{\boldsymbol{e}}^\Psi) \tag{67}$$

where the subscript k denotes the contribution made by element k. A possible adaptive algorithm is then to refine all elements k' which are such that $\Delta_{k'} \geq \theta \max_k \Delta_k$, where $\theta \in (0,1)$. The adaptive procedure is terminated when the tolerance condition $\Delta \leq \tau$ is reached. The parameters θ and τ are specified by the user. The mesh adaptivity could be achieved through enrichment with hanging nodes [24] or, perhaps, by regeneration of the complete grid. However, in the implementation followed here, adaptation is achieved by either locally increasing the polynomial order or by a local refinement that allows no hanging nodes [28].

8. EXAMPLES OF ADAPTIVE COMPUTATIONS

8.1. p Adaptation

To illustrate the effectiveness of the adaptive mesh procedure, we begin by considering problems involving the interaction between electromagnetic waves and a scatterer in the form of an infinitely thin PEC circular cylindrical cavity with an aperture. The region inside and outside the cavity consists of free space. Initially, scattering of a plane TE wave by a cavity of diameter $d = 2\lambda$ and an aperture of 45 degrees is considered. The computational domain is discretised using a structured mesh of 144 triangular elements. For this mesh, an initial distribution of p is obtained from the dispersion relationship of equation (61). The truth mesh is taken to be the same structured mesh, but with uniform order $p = 8$ elements. The adaptivity will be based upon element contributions to the computed bound gap for the value of the scattering width at the viewing angle $\phi = 0$. Starting from the initial mesh, the adaptivity procedure is employed until a tolerance level of $0.1 \times 4\sigma_H(0)/\omega$ is reached. Figure 9 shows the adaptive distributions of p which are produced by the algorithm. The initial distribution of p, shown in Figure 9 (a), contains elements of different order due to the variation in the mesh spacing over the computational domain. In Figures 9 (b)–9 (f), it can be observed that the adaptive algorithm automatically increases the order of the elements in the vicinity of the aperture. The efficiency of the computational algorithm is considered in Figure 10. This figure compares the relative bound gap, $(s^+ - s^-)/s_h$, with the number of unknowns required when adaptive p and uniform p refinements are employed. We observe that, for the same accuracy, the adaptive procedure produces discretisations which use significantly less unknowns. Contours of $Re(H_z^s)$ and $Im(H_z^s)$ for the converged solution are shown in Figure 11. The RCS distributions for uniform and adaptive p distributions are also shown and it can be observed that both distributions are in excellent agreement.

8.1.1. Electrically large objects Significant industrial attention is being devoted to the simulation of electromagnetic wave scattering by objects that are electrically large and it is of interest to examine the possibilities offered by adaptive procedures in the solution of such

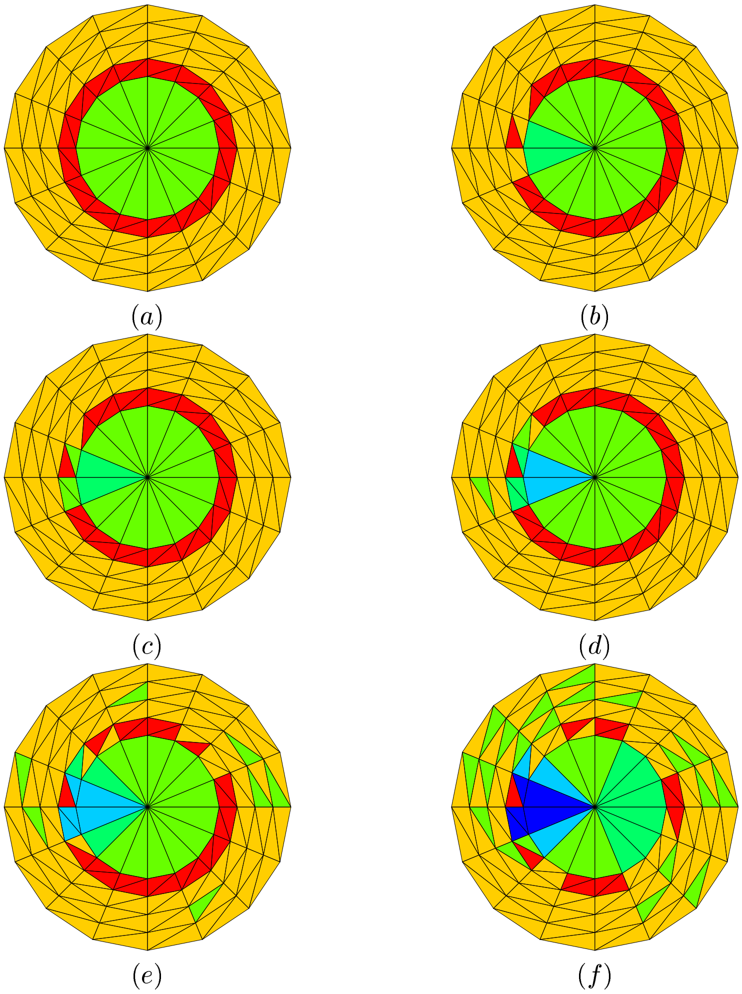

Figure 9. Scattering of a plane TE wave by a thin cylindrical PEC cavity, of electrical length 2λ and 45 degree aperture, showing the adaptive polynomial distributions obtained: (a) initial distribution from the dispersion relation, (b) first, (c) second, (d) third, (e) fourth and (f) fifth refinements, where red denotes $p = 3$, yellow $p = 4$, green $p = 5$, dark green $p = 6$, blue $p = 7$ and dark blue $p = 8$

problems. We therefore consider scattering of a plane TM wave by thin PEC cylindrical circular cavities of diameters $d = 4\lambda$, 8λ and 16λ in turn and with an aperture of 20 degrees. For each case, the convergence of the relative bound gap with the number of unknowns is shown for (a) an adaptive p procedure that starts from a coarse discretisation; (b) an adaptive procedure which uses the dispersion relation to define the distribution of the element order p on the initial mesh; and (c) the case of uniform polynomial refinement. In all cases, the objective is to terminate the adaptive procedure when the tolerance level $\tau = 0.01 \times 4\sigma_H(0)/\omega$ is reached. In addition, scattering width distributions and contour plots for the converged solutions are

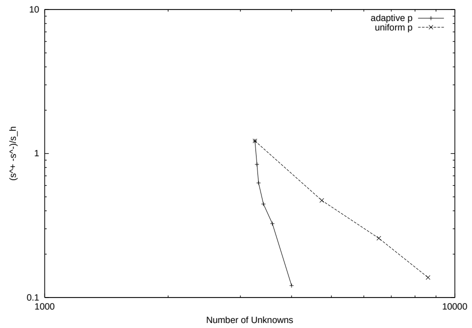

Figure 10. Scattering of a plane TE wave by a thin cylindrical PEC cavity, of electrical length 2λ and 45 degree aperture, showing the convergence of the relative bound gap $(s^+ - s^-)/s_h$ with the number of unknowns, when uniform p and adaptive p refinement strategies are employed

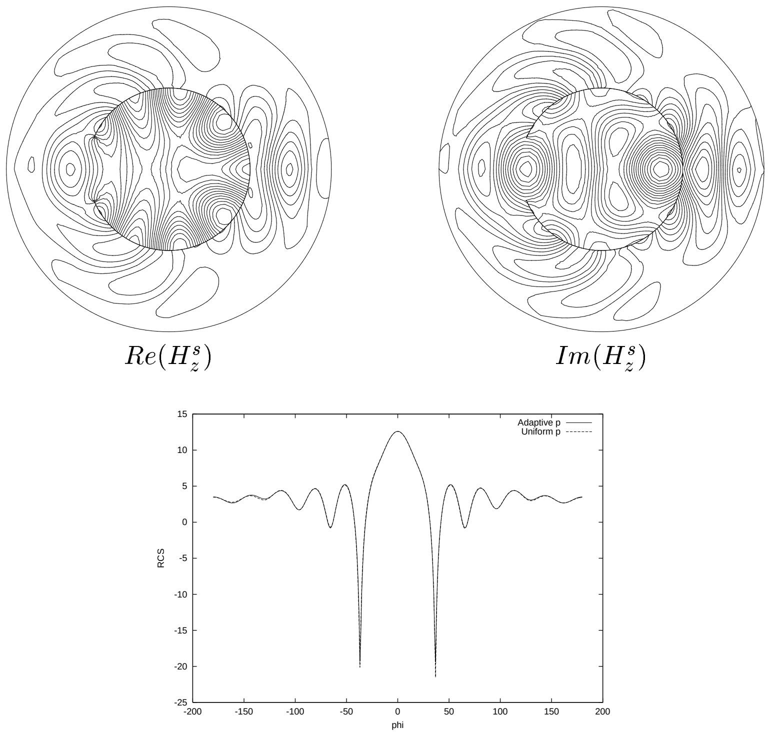

Figure 11. Scattering of a plane TE wave by a thin cylindrical PEC cavity, of electrical length 2λ and aperture 45 degrees, showing contours of $Re(H_z^s)$ and $Im(H_z^s)$ and the computed distribution of the scattering width for the converged solutions

presented.

For the case $d = 4\lambda$, Figure 12 shows the convergence of the relative bound gap for the different adaptive strategies. The truth mesh for this problem has elements of uniform order $p = 8$. When the adaptive p procedure is initiated on a coarse discretisation, the convergence path is initially the same as that produced by uniform p refinement. However, these curves ultimately diverge and the adaptive p procedure then produces solutions of the same accuracy with fewer unknowns. It should be emphasized that the bounds that are obtained in these calculations always bound the true solution and that, although the bounds are quantitatively very large on very coarse discretisations, the bound gap decreases as the discretisations become finer. When the dispersion relation is employed to define the variation of the element order on the initial mesh, fewer adaptations are required to reach a desired tolerance. The 19 640 unknowns which are finally used in the case of adaptive p refinement is very similar to the 20 611 unknowns which are required when the dispersion relationship is employed. Contours of the computed solution and the converged scattering width distribution are shown in Figure 13.

Next we consider the scattering of a plane TM wave when the cavity diameter is $d = 8\lambda$. For this case, the truth discretisation has been selected to have elements of uniform order $p = 10$. Figure 14 shows the convergence of the relative bound gap for a selection of adaptive strategies. It may be observed that, when the adaptive p strategy is initiated on a very coarse discretisation, the convergence behaviour is initially rather erratic, with the relative bound gap decreasing and then increasing. However, following a few further adaptive steps, the procedure settles down and ultimately produces a solution in which the number of unknowns required is less than that obtained with uniform refinement. When the dispersion relationship is employed to generate an initial p distribution, the convergence is rapid and without oscillation. As in the $d = 4\lambda$ case, the number of unknowns used in the two adaptive procedures is again very similar. Contours of the computed solution and the converged scattering width distribution for this case are shown in Figure 15.

Finally, we consider the scattering of a plane TM wave when the diameter of the cavity is $d = 16\lambda$. For this case, Figure 16 shows the convergence of the relative bound gap. The truth discretisation for this problem has uniform order $p = 14$ elements. When the adaptive p strategy is initiated on a coarse discretisation, the convergence behaviour is very erratic and is characterised by wild increases and decreases in the size of the bound gap. After 15 adaptive steps, no convergence is apparent and the adaptive strategy is stopped. When uniform p refinement is employed, the solution convergence is found to be uniform throughout. The adaptivity strategy which uses the dispersion relationship to obtain an initial distribution of $p = 10$ elements is observed to produce solutions requiring less unknowns than uniform p refinement. These results suggest that, as the electrical length of the scatterer increases, it is essential to use the dispersion relationship to create a meaningful starting point for the adaptive procedure. To complete this example, we show the contours of $Re(E_z^s)$ and $Im(E_z^s)$ and plot the distribution of the scattering width in Figure 17.

8.2. *h* Adaptation

When strong singularities are present in a problem, the best adaptive mesh approach is often to employ some form of h adaptation in the vicinity of the singularities to localise their effects [21]. We now include an example that demonstrates how h adaptation can be used to adaptively improve the bounds on the output $4\sigma_H(0)/\omega$. The example chosen is the scattering

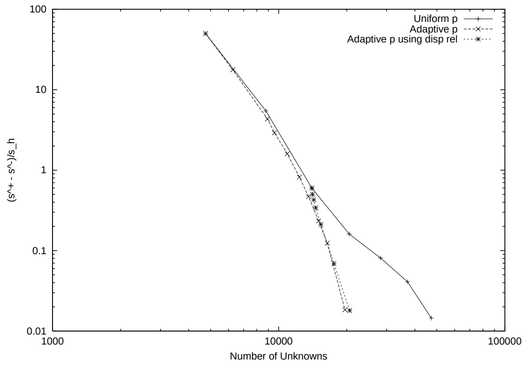

Figure 12. Scattering of a plane TM wave by a thin cylindrical PEC cavity, of diameter $d = 4\lambda$ and aperture 20 degrees, showing the convergence of the relative bound gap $(s^+ - s^-)/s_h$ with number of unknowns when uniform p and adaptive p refinement strategies are employed

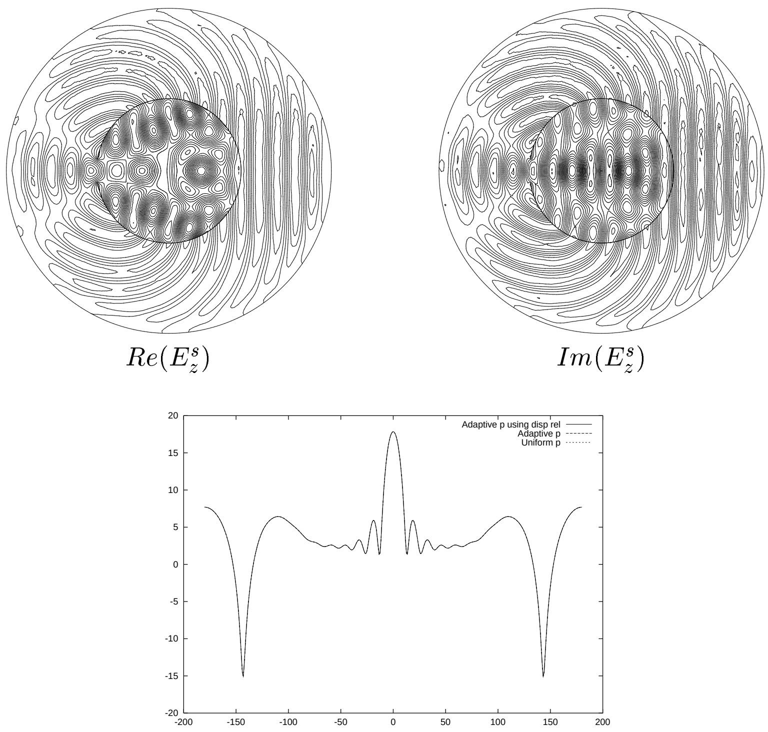

Figure 13. Scattering of a plane TM wave by a thin cylindrical PEC cavity, of diameter $d = 4\lambda$ and aperture 20 degrees, showing contours of $Re(E_z^s)$ and $Im(E_z^s)$ and the computed distribution of the scattering width for the converged solution

Prepared using fldauth.cls

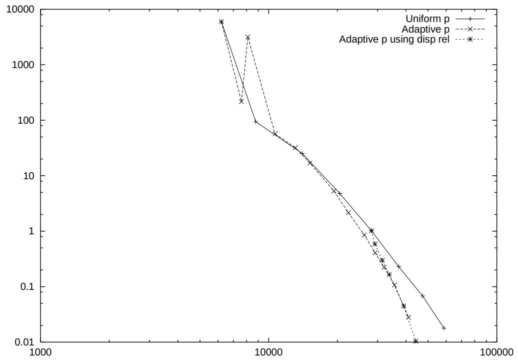

Figure 14. Scattering of a plane TM wave by a thin cylindrical PEC cavity, of diameter $d = 8\lambda$ and aperture 20 degrees, showing the convergence of the relative bound gap $(s^{+} - s^{-})/s_h$ with number of unknowns when uniform p and adaptive p refinement strategies are employed

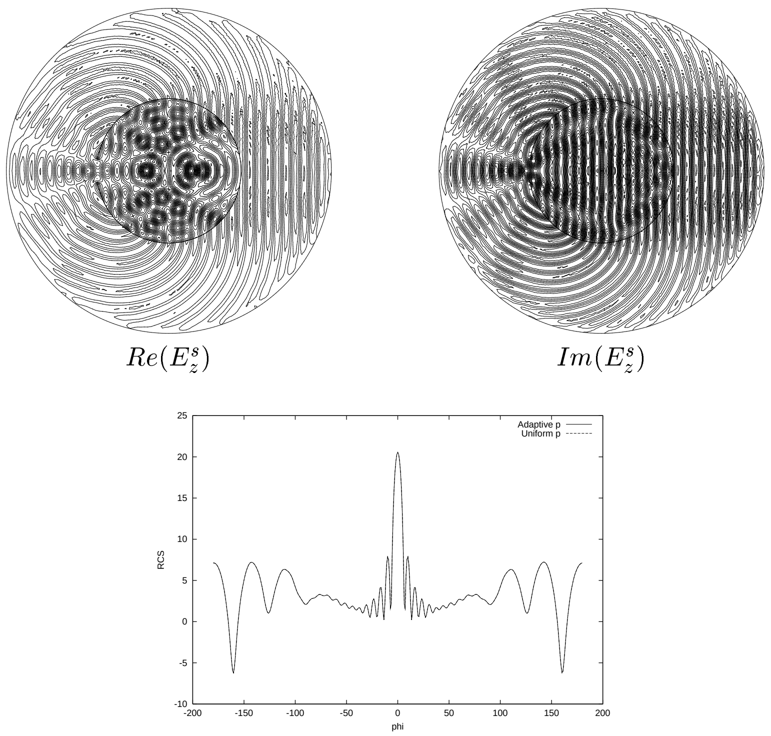

Figure 15. Scattering of a plane TM wave by a thin cylindrical PEC cavity, of diameter $d = 8\lambda$ and aperture 20 degrees, showing contours of $Re(E_z^s)$ and $Im(E_z^s)$ and the computed distribution of the scattering width for the converged solution

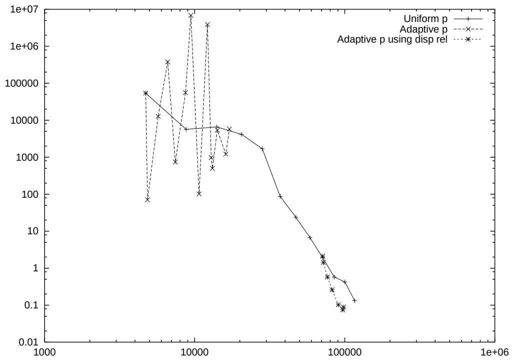

Figure 16. Scattering of a plane TM wave by a thin cylindrical PEC cavity, of diameter $d = 16\lambda$ and aperture 20 degrees, showing the convergence of the relative bound gap $(s^+ - s^-)/s_h$ with number of unknowns when uniform p and adaptive p refinement strategies are employed

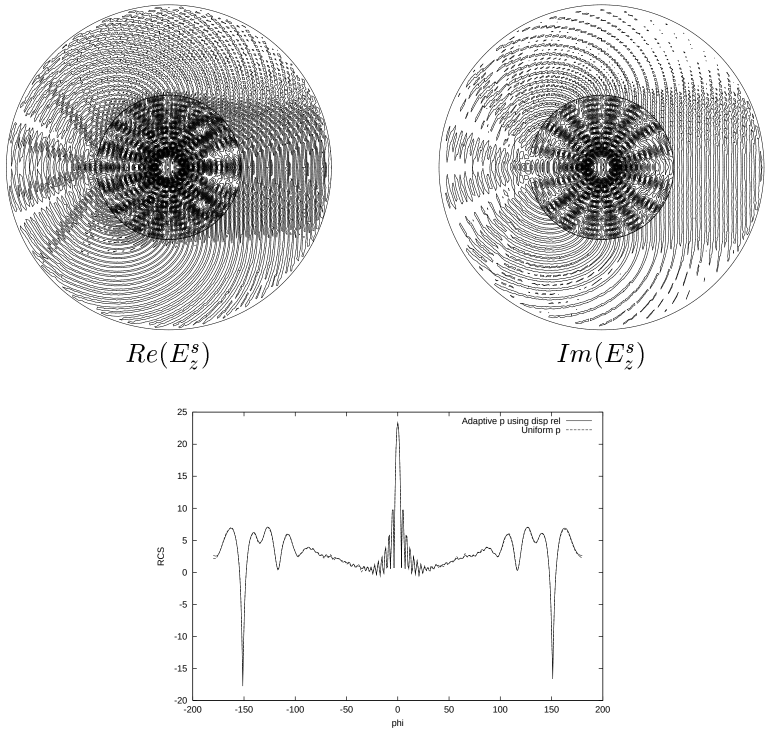

Figure 17. Scattering of a plane TM wave by a thin cylindrical PEC cavity, of diameter $d = 16\lambda$ and aperture 20 degrees, showing contours of $Re(E_z^s)$ and $Im(E_z^s)$ and the computed distribution of the scattering width for the converged solution

of a plane TE wave by a U shaped PEC cavity which has been rotated through 90 degrees. The thickness of the walls of the cavity is denoted by t and the outer dimensions are given by $b+t$ in the x direction and $c+2t$ in the y direction. The implication here is the cavity has inner dimensions b and c. We consider, in particular, the cavity which is defined by the specific values $t = 0.2\lambda = 0.2$ $b = 4\lambda = 0.4$ and $c = 2\lambda = 1$. This geometry is slightly more complicated than those used previously and, in this case, the initial mesh of triangles is created by an unstructured mesh generator. For the PML, a structured layer of quadrilaterals is added to produce a hybrid mesh [9]. The use of quadrilateral elements requires a modification to the error estimating procedure, but the theory can be developed in a manner very similar to that described above for triangles [22]. However, in these h adaptive computations, the h refinement is restricted to the unstructured mesh region, and the quadrilaterals in the PML are left unaltered. The selected tolerance level is $\tau = 0.03 \times 4\sigma_H(0)/\omega$.

Figure 18 displays the series of adaptive meshes that are produced. The initial mesh has 44 quadrilateral and 407 triangles and is shown in Figure 18 (a). The dispersion relation indicates that uniform order $p = 3$ elements should be employed. The adaptive meshes shown in Figure 18 (b)–18 (e) illustrate how the error estimator flags the elements close to the singular points for refinement. The elements are refined in these regions until the truth spacing of $h = 0.1$ is reached. Figure 19 shows a plot of the computed relative bound gap against the number of unknowns for the adaptive h and uniform h refinements. In this figure, it observed that employing the adaptive h refinement procedure requires less unknowns than the uniform h refinement procedure. Contours of the converged solution, together with the computed distribution of the scattering width, can be found in Figure 20. In particular, the scattering width distributions given by the adaptive h and the uniform h refinement are found to be in excellent agreement.

9. CONCLUSIONS

This paper has demonstrated an implementation of a procedure for computing bounds on the outputs of electromagnetic wave scattering problems in the frequency domain by using an extension of the approach of Patera and Peraire. The solution is achieved by means of a Galerkin finite element approximation, using arbitrary order edge elements and with the far field boundary condition imposed by using a PML. Of particular importance is the demonstration of the practicality of using the proposed method to obtain bounds on the scattering width distribution.

10. ACKNOWLEDGEMENTS

Paul Ledger acknowledges the support of EPSRC in the form of a PhD studentship under grant GR59/M59112. Jaime Peraire acknowledges the support of EPSRC in the form of a visiting fellowship award under grant GR/N09084.

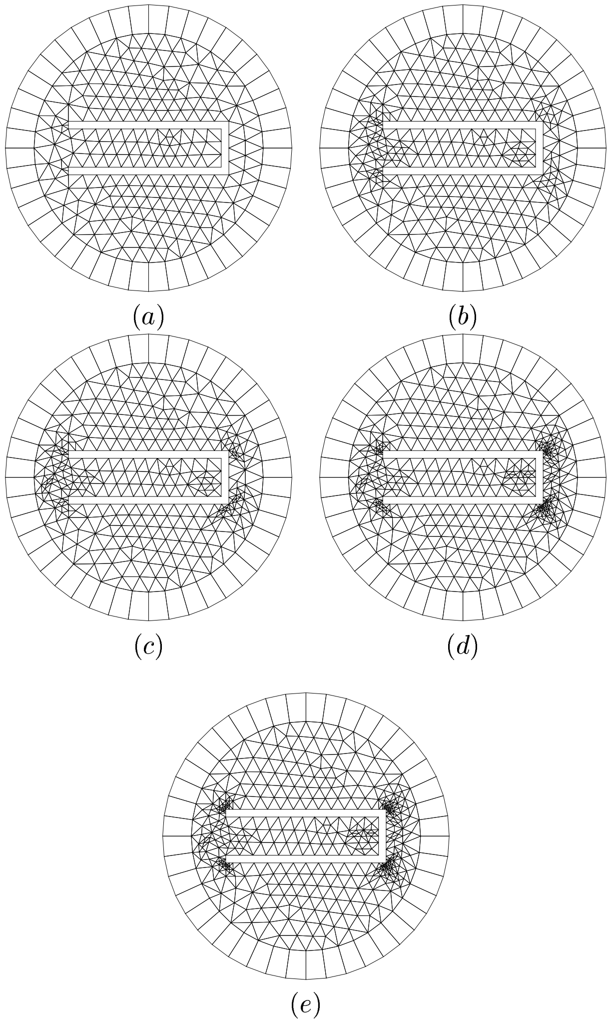

Figure 18. Scattering of a plane TE wave by a PEC cavity of length 4λ showing (a) the initial mesh and (b) the first, (c) the second, (d) the third and (e) the fourth mesh refinements

REFERENCES

1. Nédélec JC. Computation of eddy currents on a surface in $\mathbb{R}^3$ by finite element methods. *SIAM Journal of Numerical Analysis* 1978;**15**:580–594.
2. Nédélec JC. Mixed finite elements in $\mathbb{R}^3$. *Numerische Mathematik* 1980;**35**:315–341.
3. Nédélec JC. A new family of mixed finite elements in $\mathbb{R}^3$. *Numerische Mathematik* 1986;**50**:57–81.
4. Monk P. An analysis of Nédélec's method for the spatial discretisation of Maxwell's equations. *Journal of Computational and Applied Mathematics* 1993;**47**:101-121.
5. Monk P. On the $p-$ and hp–extension of Nédélec's curl conforming elements. *Journal of Computational and Applied Mathematics* 1994;**53**:117–137.
6. Demkowicz L, Rachowicz W. A 2D hp–adaptive finite element package for electromagnetics (2Dhp90em).

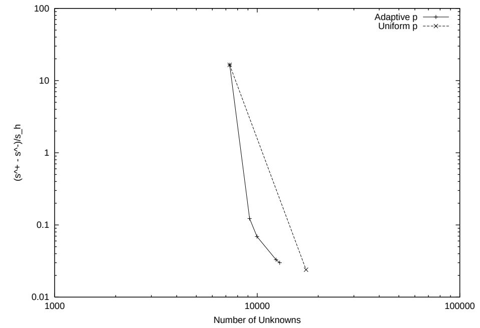

Figure 19. Scattering of a plane TE wave by a PEC cavity of length 4λ showing the convergence of the relative bound gap $(s^+ - s^-)/s_h$ with number of unknowns when uniform h and adaptive h refinements are employed

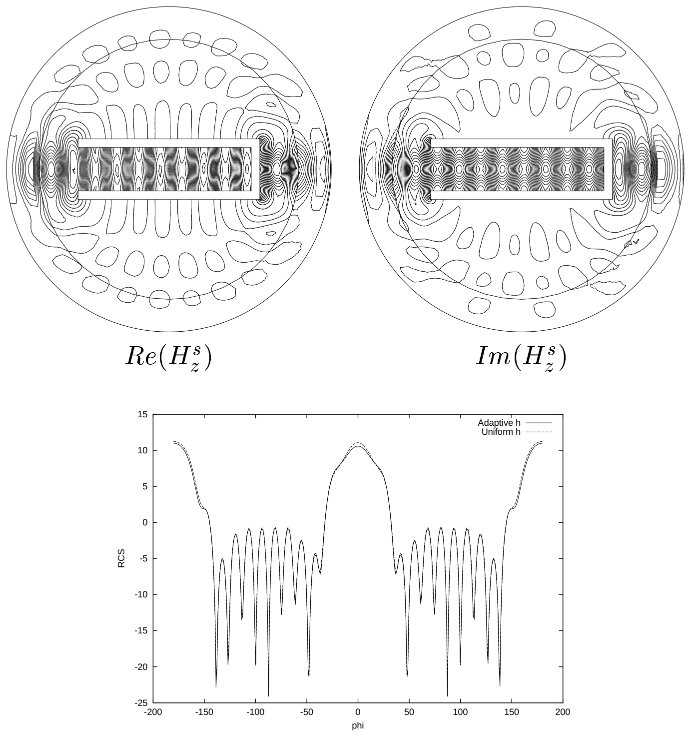

Figure 20. Scattering of a plane TE wave by a PEC cavity of length 4λ showing contours of $Re(H_z^s)$ and $Im(H_z^s)$ and the computed distribution of the scattering width for the converged solution

TICAM Report 98–15 University of Texas at Austin, 1998.
7. Demkowicz L, Vardapetyan L. Modeling of electromagnetic/scattering problems using *hp*–adaptive finite elements. *Computer Methods in Applied Mechanics and Engineering* 1998;**152**:103–124.
8. Ainsworth M, Coyle J. Hierarchic *hp*–edge element families for Maxwell's equations on hybrid quadrilateral/triangular meshes. *Computer Methods in Applied Mechanics and Engineering* 2001; **190**:6709–6733.
9. Ledger PD, Hassan O, Morgan K, Weatherill NP. PML and arbitrary order edge elements for electromagnetic scattering simulation. *International Journal for Numerical Methods in Engineering*, In press 2002.
10. Paraschivoiu M, Peraire J, Patera AT. A–posteriori finite element bounds for linear functional outputs of elliptic partial differential equations. *Computer Methods in Applied Mechanics and Engineering* 1997;**150**: 289–312.
11. Maday Y, Peraire J, Patera AT. A general formulation for a–posteriori bounds for output functionals of partial differential equations: application to the eigenvalue problem. *C.R. Acad. Sci. Paris* 1999;**328** Ser.I: 823–828.
12. Peraire J, Patera AT. Asymptotic a–posteriori finite element bounds for the outputs of noncoercive problems: the Helmholtz and Burger's equations. *Computer Methods in Applied Mechanics and Engineering* 1999;**171**:77–86.
13. Sarrate J, Peraire J, Patera AT. A–posteriori error bounds for nonlinear outputs of the Helmholtz equation. *International Journal for Numerical Methods in Fluids* 1999; **31**: 17-36.
14. Berenger J–P. A perfectly matched layer for the absorption of electromagentic waves. *Journal of Computational Physics* 1994;**114**:185–200.
15. Ledger PD. Edge elements for waveguide and scattering problems. *MSc Thesis*, University of Wales, Swansea, 1999.
16. Webb JP, Forghani B. Hierarchical scalar and vector tetrahedra. *IEEE Transactions on Magnetics* 1993;**29**:1495–1498.
17. Abramowitz M, Stegun IA. *Handbook of Mathematical Functions with Formulas, Graphs and Mathematical Tables.* National Bureau of Standards, Washington D.C., 1964.
18. Kuzuoglu M, Mittra R. Investigation of nonplanar perfectly matched absorber for finite element mesh truncation. *IEEE Transactions on Antennas and Propagation* 1997;**45**:474–486.
19. Stratton JA. *Electromagnetic Theory.* McGraw–Hill, New York, 1941.
20. Szabó B, Babuska I. *Finite Element Analysis*, John Wiley and Sons, New York, 1991.
21. Ainsworth M, Senior B. Aspects of an adaptive hp–finite element method: adaptive strategy, conforming approximation and efficient solvers. *Computer Methods in Applied Mechanics and Engineering* 1997; **150**:65–87.
22. Ledger PD. *PhD Thesis*, University of Wales, Swansea, 2002.
23. Demkowicz L. A–posteriori error analysis for steady state Maxwell's equations. In Ladaveze, P., Oden JT. (editors), *New Advances in Adaptive Computational Methods in Mechanics*, Elsevier, New York 1998.
24. Peraire J, Patera AT. Bounds for linear functional outputs of coercive partial differential equations: local indicators and adaptive refinement. In Ladaveze, P., Oden JT. (editors), *New Advances in Adaptive Computational Methods in Mechanics*, Elsevier, New York 1998.
25. Monk P. The near to far field transformation. *International Journal for Computation and Mathematics in Electrical and Electronic Engineering* 1995;**14**:41–56.
26. Monk P, Suli E. The adaptive computation of far field patterns by a–posteriori error estimation of linear functionals. *SIAM Journal of Numerical Analysis* 1998;**36**: 251–274.
27. Monk P, Parott K. Phase accuracy and improved farfield estimates for 3–D edge elements on tetrahedral meshes. *Journal of Computational Physics* 2001;**170**:614-641.
28. Löhner R, Morgan K, Zienkiewicz OC. Adaptive grid refinement for the compressible Euler equations. In Babuska I. et al. (editors), *Accuracy Estimates and Adaptive Refinements in Finite Element Computations*, 281–297, John Wiley, Chichester, 1986.